



## Microstructure evolution and mechanical properties of laser additive manufactured Ti–5Al–2Sn–2Zr–4Mo–4Cr alloy

Qiang ZHANG, Jing CHEN, Hua TAN, Xin LIN, Wei-dong HUANG

State Key Laboratory of Solidification Processing, Northwestern Polytechnical University, Xi'an 710072, China

Received 21 July 2015; accepted 10 November 2015

**Abstract:** The microstructure, microhardness and tensile properties of laser additive manufactured (LAM) Ti–5Al–2Sn–2Zr–4Mo–4Cr alloy were investigated. The result shows that the microstructure evolution is strongly affected by the thermal history of LAM process. Primary  $\alpha$  ( $\alpha_p$ ) with different morphologies, secondary  $\alpha$  ( $\alpha_s$ ) and martensite  $\alpha'$  can be observed at different positions of the LAMed specimen. Annealing treatment can promote the precipitation of rib-like  $\alpha$  phase or acicular  $\alpha$  phase. As a result, it can increase or decrease the microhardness. The as-deposited L-direction and T-direction specimens contain the same phase constituent with different morphologies. The tensile properties of the as-deposited LAMed specimens are characterized of anisotropy. The L-direction specimen shows the character of low strength but high ductility when compared with the T-direction specimen. After annealing treatment, the strength of L-direction specimen increases significantly while the ductility reduces. The strength of the annealed T-direction specimen changes little, however, the ductility reduces nearly by 50%.

**Key words:** Ti–5Al–2Sn–2Zr–4Mo–4Cr alloy; laser additive manufacture; microstructure; thermal history; mechanical properties

### 1 Introduction

Ti–5Al–2Sn–2Zr–4Mo–4Cr alloy, researched and developed in 1970s by GE, is classified as “ $\beta$ -rich”  $\alpha+\beta$  alloy. It is widely used for gas turbine engine component, such as disks for fan and compressor stages because of its characters of high-strength, deep hardenable and high-toughness [1,2].

Laser additive manufacture (LAM) is an advanced processing technology that can be used to fabricate 3D near-net shape metal components directly [3–5]. During LAM process, metal powders are fed into the molten pool on the substrate produced by the laser irradiation and the injected powders re-solidify after melting. The laser beam or working table moves along the pre-designed paths, thus, 3D metal parts without any tooling are fabricated layer by layer. The LAM process offers distinct advantages over conventional manufacturing, such as free of tooling, high design freedom and short lead time. The LAM process is particularly appealing for fabrication of expensive and unworkable titanium aerospace components. Lots of

studies focused on microstructure evolution of LAMed titanium alloy have been carried out. Typical macrostructure of LAMed  $\alpha+\beta$  titanium alloy is usually comprised of columnar  $\beta$  grains which grow epitaxially from the substrate [6–8]. The  $\alpha$  phase precipitated in the  $\beta$  matrix during cooling shows more complex features, such as fine lamellar structure containing martensitic  $\alpha'$  [9], coarsen lamellar structure [10] and layer bands [11–13]. Researches on near  $\beta$  titanium alloys, such as Ti–5Al–5Mo–5V–1Cr–1Fe alloy, have revealed that the deposited sample fabricated under the same process parameters can exhibit more complex microstructure characterization due to the more complex alloy ingredients. As reported by LIU et al [14], ultra-fine  $\alpha$  laths, coarse  $\alpha$  laths and ultra-fine basket-weave  $\alpha$  can be obtained [14]. As well documented that the mechanical properties of titanium alloy components are strongly affected by the microstructures characterizations [15]. In other words, different microstructures and mechanical properties may be achieved even though the titanium components with different sizes and shapes were fabricated by the same processing parameters due to the different thermal

history they experienced. However, little work focusing on this effect has been conducted.

In this study, the samples with different dimensions were fabricated under the same processing parameters. The effects of dimensions and annealing treatment on the microstructure characterization were investigated. Besides, the microhardness and room temperature tensile properties of the as-deposited and annealed specimens were also examined.

## 2 Experimental

All the samples were fabricated by an LAM equipment which consists of a 4 kW continuous wave CO<sub>2</sub> laser, a 5-axis numerical control working table, an inert gas chamber filled with pure argon and a coaxial powder feeder nozzle.

The Ti–5Al–2Sn–2Zr–4Mo–4Cr alloy powders with the sizes of 80–120 μm were used as cladding materials. The powders were dried in a vacuum oven at (120±5) °C for 2 h to eliminate moisture absorption. The LAM processing parameters, laser power (LP), scanning speed (SS), powder federate (PF), spot diameter (SD) and overlaps (OL), are shown in Table 1.

**Table 1** Processing parameters of LAM process

LP/kW	SS/(mm·s <sup>-1</sup> )	PF/(g·min <sup>-1</sup> )	SD/mm	OL/%
2.5–2.8	8–10	3–5	2–3	40

Two solid structures with dimensions of 10 mm × 10 mm × 5 mm and 10 mm × 10 mm × 25 mm were fabricated on the surface of the forged Ti–5Al–2Sn–2Zr–4Mo–4Cr alloy plate. The as-deposited samples were sectioned into 4 pieces along the direction perpendicular to the laser scanning direction. One of them was used as as-deposited state sample, and others were annealed with different heat treatment routes: 600 °C, 1 h/FC (furnace cooling); 600 °C, 2 h/FC; 600 °C, 4 h/FC. Metallographic specimens for scanning electron microscopy (SEM, Tescan VEGA II LMH) were prepared by mechanical polishing and revealed by a solution of 2 mL HF, 6 mL HNO<sub>3</sub> and 100 mL H<sub>2</sub>O. Thin foils for transmission electron microscopy (TEM) were prepared by electro-polishing using a double jet apparatus with a solution of 300 mL methanol, 180 mL butanol and 30 mL perchloric acid at a potential of 15 V DC. The phase constitution was analyzed by X-ray diffraction (XRD, Bruker D8 Advance). The microhardness from the bottom to the top of the specimens along the building direction was measured on a Duranmin–A300 microhardness tester after the samples were re-polished. The test was carried out with the load of 5 N and the load time of 15 s and the interval between two indentations was 0.5 mm.

The blocky samples used for tensile test were deposited on the surface of the titanium plates. As shown in Fig. 1(a), the specimen with the loading direction parallel to the building direction is labeled as L-direction specimen and the specimen with the loading direction perpendicular to the building direction is labeled as T-direction. After heat treatment at 600 °C for 1 h followed by furnace cooling, the samples were machined to standard tensile specimens (Fig. 1(b)) according to GB/T228 and tested on an Instron 5982 tensile machine. The as-deposited specimens were also tested under the same condition in order to compare with the annealed specimens. The tensile fracture surfaces and cross-sections of the tensile specimens were examined using a scanning electron microscope.

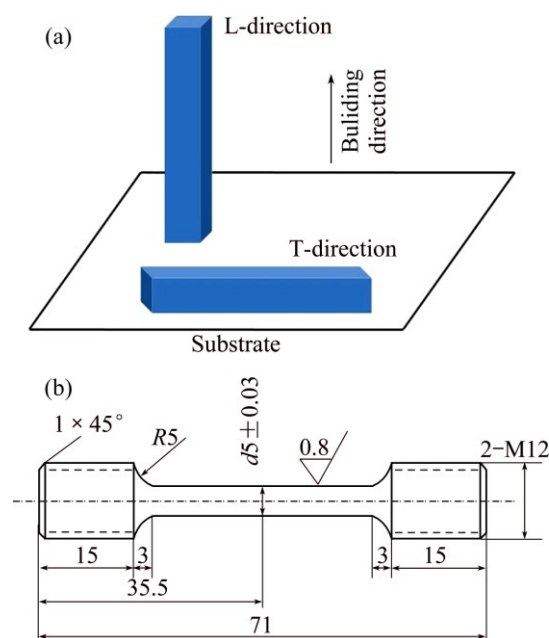


**Fig. 1** Schematic of L-direction and T-direction specimens (a) and standard tensile specimen (b) (unit: mm)

## 3 Results and discussion

### 3.1 Microstructure characteristics of as-deposited samples

The microstructures of the 5 mm as-deposited sample are shown in Fig. 2. The microstructures are obviously different according to the positions. At the bottom of the sample, very fine basket-weave  $\alpha$  phase can be observed (Fig. 2(a)). However, at the top of the sample, acicular martensite  $\alpha'$  can be observed in the TEM image (Fig. 2(b)). The results of XRD analysis of the as-deposited and 4 h annealed samples are shown in Fig. 2(c). The much wider  $\alpha$  peaks of the as-deposited sample identify the presence of martensite structure ( $\alpha'$ ).

Figure 3 shows the SEM images of the 25 mm as-deposited sample from the bottom to the top along the

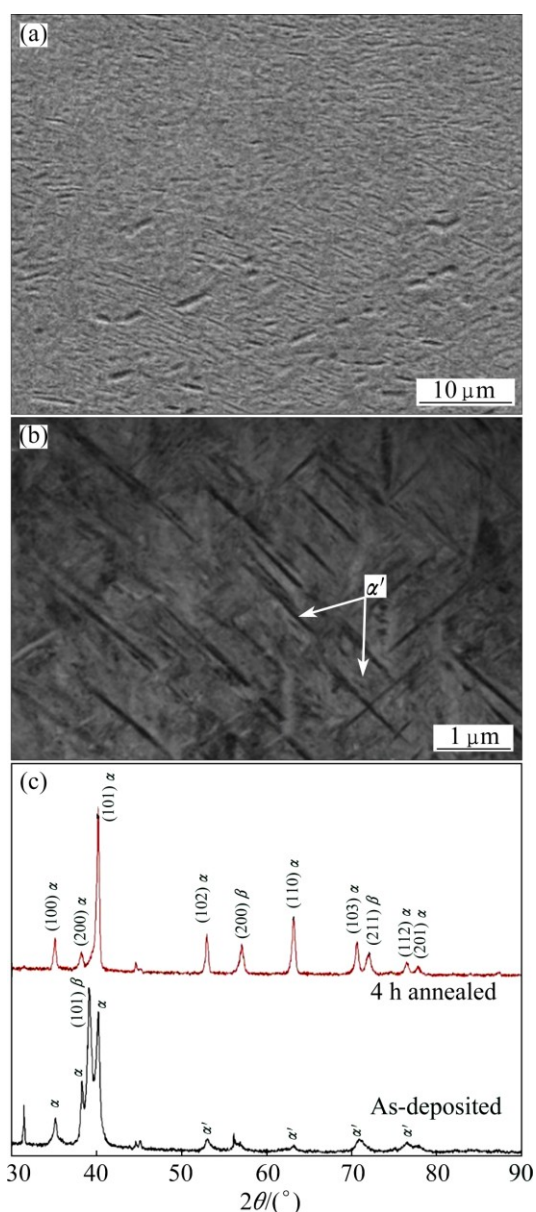


**Fig. 2** Microstructures of 5 mm as-deposited sample: (a) SEM image of bottom of deposited layers; (b) TEM image of top of deposited layers; (c) XRD patterns of as-deposited and 4 h annealed samples

building direction. It can be found that the microstructures change considerably compared with the as-deposited 5 mm specimen. The amount and the morphology of  $\alpha$  phase change notably along the building direction. Very fine basket-weave microstructure can be observed at the bottom of the sample, as shown in Fig. 3(a). Near the bottom of the specimen, irregularly primary  $\alpha$  phase ( $\alpha_p$ ) and fine secondary  $\alpha$  phase ( $\alpha_s$ ) can be seen in Fig. 3(b). Away from the bottom of the sample, only  $\alpha_p$  can be observed (Fig. 3(c)). At the top of the specimen, there is no  $\alpha$  phase (Fig. 3(d)).

The microstructure evolution is considered to

depend on the thermal history of the LAM process. Thermal history during LAM process was simulated by adopting the birth and death technology and the enthalpy potential method. The finite-element model was discussed in another study [16] and the same physical parameters were adopted. Figures 4(a) and (b) show the simulation results of temperature distribution when the 5 and 25 mm samples are finished. It can be seen that the temperature distribution of the samples is not uniform. The temperature at the top of the sample is the highest and reduces gradually from the top to the bottom. It should be noted that the temperature of the 25 mm sample is higher than that of the 5 mm specimen due to the heat accumulation which may lead to a faster cooling rate at the beginning of cooling process.

Combined with the previous studies [14,17] and the observed microstructure in this study, the microstructure evolution is schematically illustrated in Fig. 4(c). At the top of the sample, where the temperature is higher than the  $\beta$  transus temperature ( $T_\beta$ ), solution treatment occurs in single  $\beta$  phase region. Due to the high  $\beta$  stabilization in Ti-5Al-2Sn-2Zr-4Mo-4Cr alloy and air cooling after the LAM process, the formation of  $\alpha$  phase is suppressed, and martensite  $\alpha'$  in 5 mm specimen and metastable  $\beta$  phase ( $\beta_m$ ) in 25 mm specimen are obtained. As described by SAUER and LUETJERING [18], high temperature aging will form coarse  $\alpha$ -plates throughout the  $\beta$  matrix. During low temperature aging, a high volume fraction of fine secondary  $\alpha$ -plates is precipitated in the  $\beta$  matrix. So at a lower position, both coarse and fine  $\alpha$  phase can be observed with the decrease of temperature in LAMed specimen.

For the 5 mm sample, only at the bottom of the sample, the temperature is below  $T_\beta$ , while the temperature at most part of the sample is close to or above  $T_\beta$ . So, if the process ends, the transformation of  $\beta$  to  $\alpha$  would be suppressed due to the quick cooling rate. The microstructure similar to the 5 mm sample would be achieved. If the LAM process continues, an obvious temperature gradient in the sample will form, as approximately illustrated in Fig. 4(c). It is widely accepted that as the temperature reduces in the  $\alpha+\beta$  phase field, the volume fraction of  $\alpha$  phase increases [18] and this can be confirmed in Fig. 3. Besides, a series of phase transformations, such as  $\beta \rightarrow \alpha'$  or  $\beta_m$ , and  $\alpha'$  or  $\beta_m \rightarrow \alpha+\beta$  happen. As a result, very diverse microstructures can be obtained in the 25 mm sample.

### 3.2 Microstructure characteristics of annealed samples

The microstructures of the annealed 5 mm sample are shown in Fig. 5. As shown in Fig. 5(a), the size of fine acicular  $\alpha$  phase at the bottom of the sample changes

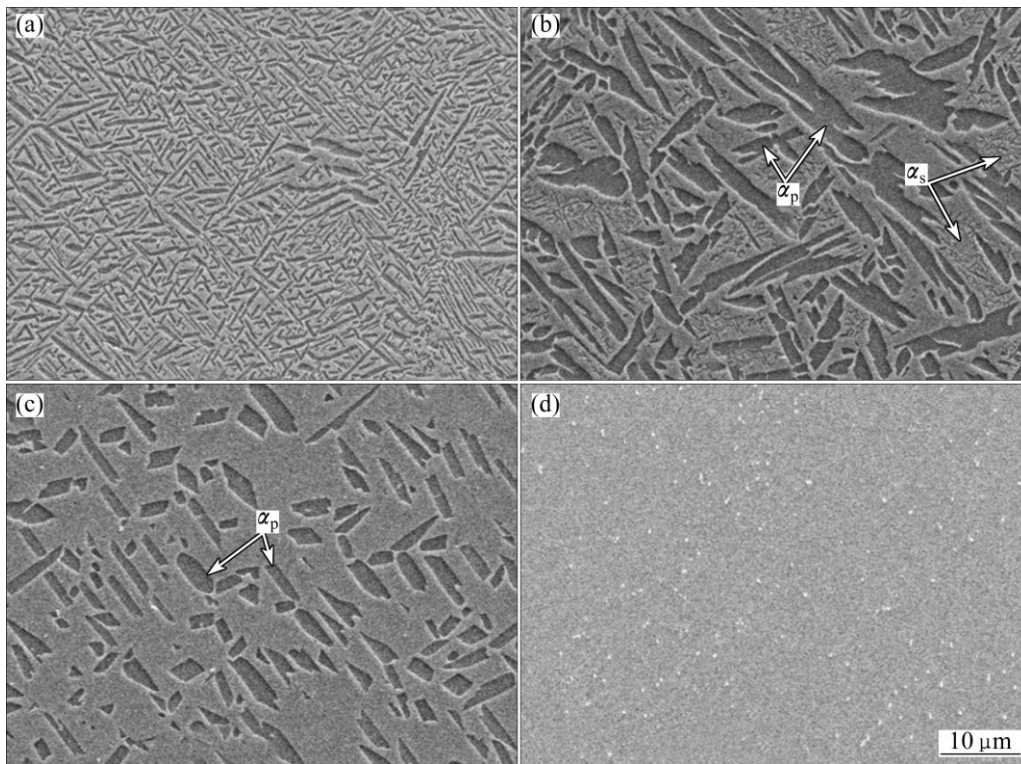


Fig. 3 Microstructures at bottom (a), middle (b, c) and top (d) of 25 mm as-deposited sample

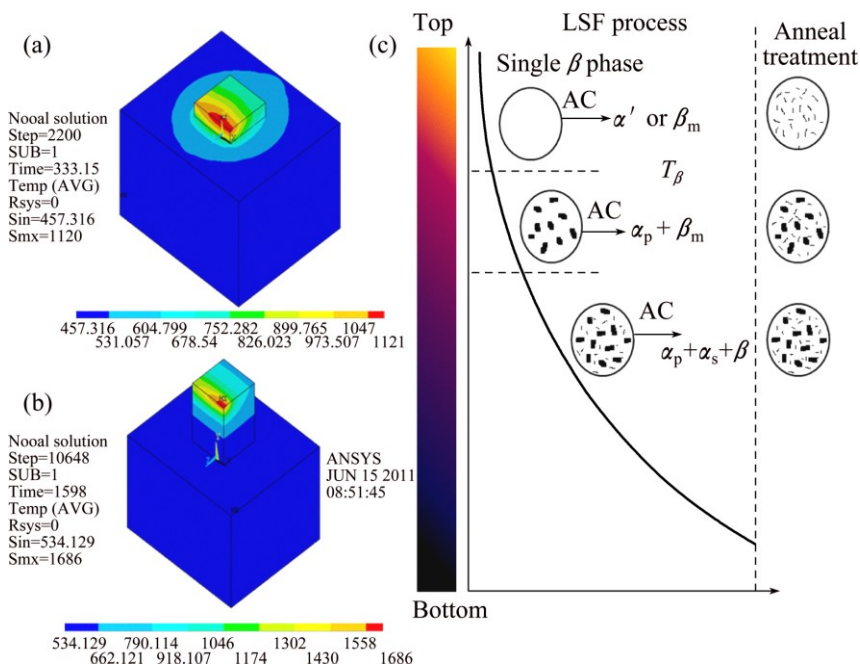
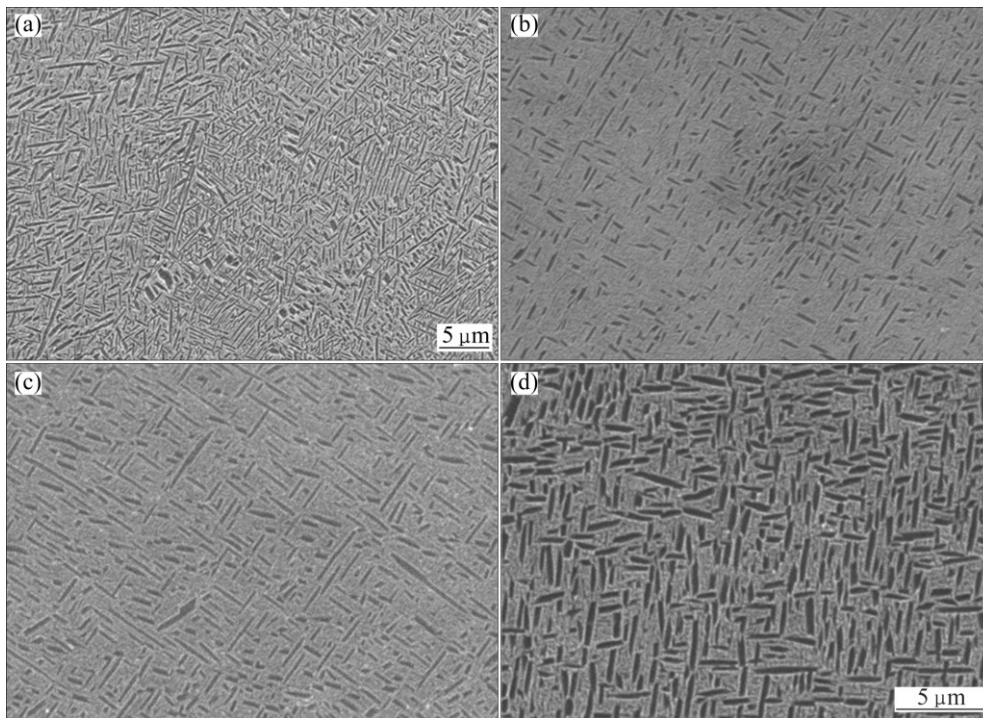


Fig. 4 Simulation results of ANSYS: (a) Temperature distribution of 5 mm sample; (b) Temperature distribution of 25 mm sample; (c) Schematic of microstructure evolution

a little after 1 h annealing treatment. However, at the top of the sample, martensite  $\alpha'$  is replaced by rib-like  $\alpha$  phase (less than 2  $\mu\text{m}$ ) and extremely fine  $\alpha_s$ , as shown in Fig. 5(b). As shown in Figs. 5(c) and (d), the rib-like  $\alpha$  phase becomes coarsening with prolonging the time. The phase constituent of the 4 h annealed specimen was

analyzed by XRD and the result is shown in Fig. 2(c). As shown in Fig. 2(c), there is no martensite  $\alpha'$ .

As shown in Figs. 6(a) and (b), annealing treatment does not impact the microstructure significantly at lower half part of the 25 mm specimen. There is still no noticeable change when the annealing time extends to



**Fig. 5** Microstructures of annealed 5 mm specimen: (a) Bottom of 1 h annealed specimen; (b) Top of 1 h annealed specimen; (c) Top of 2 h annealed specimen; (d) Top of 4 h annealed specimen

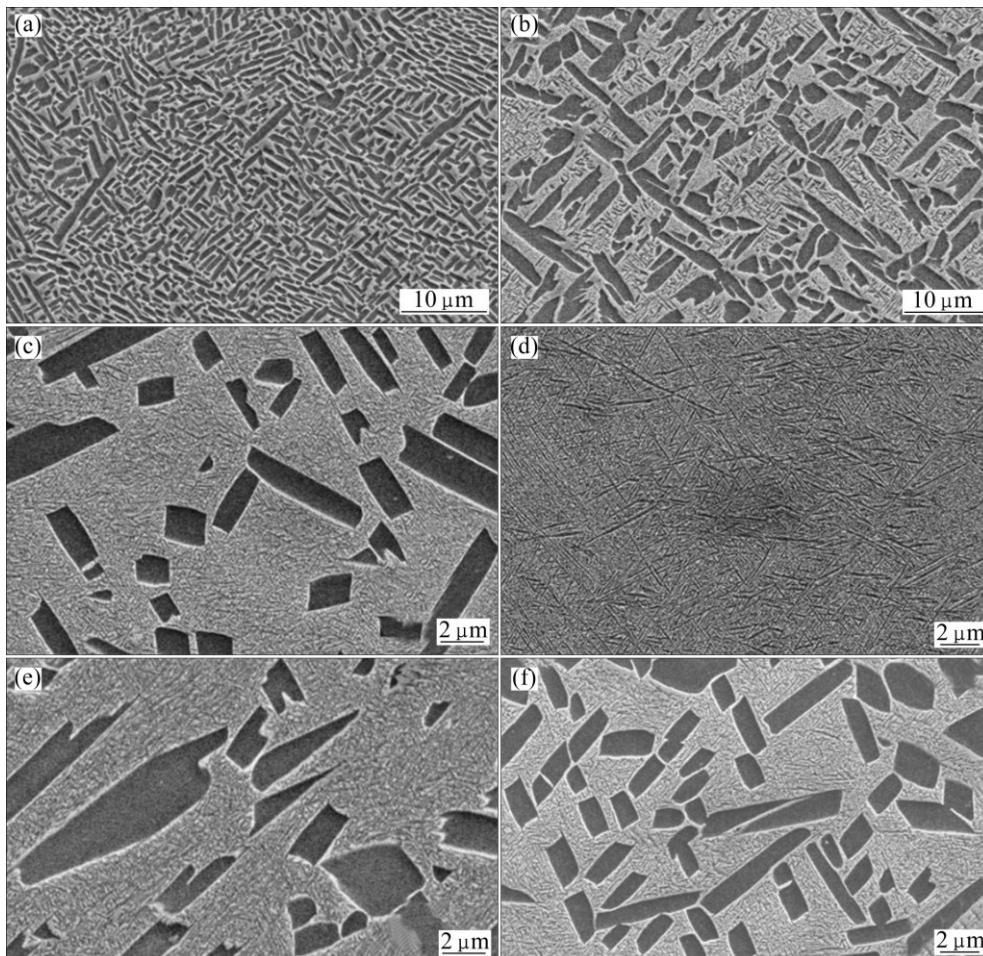


**Fig. 6** Microstructure evolution along building direction of annealed 25 mm sample: (a)–(d) Microstructures from bottom to top of 1 h annealed sample; (e) and (f) Microstructures corresponding to Fig. 6(c) after 2 h and 4 h annealing treatments, respectively

2 and 4 h. This is because  $\alpha$  phase precipitates from  $\beta$  phase adequately during the LAM process. However, as shown in Fig. 6(c), at upper half part of the sample, fine  $\alpha_s$  precipitates directly from the metastable  $\beta$  phase. At the top of the sample, acicular  $\alpha$  can be observed. It can be seen from Figs. 6(e) and (f), the microstructure does not change apparently when the annealing time extends to 2 and 4 h.

### 3.3 Microhardness of as-deposited and annealed samples

The microhardness of as-deposited and annealed samples (5 and 25 mm samples) along the building direction is shown in Fig. 7. For the 5 mm sample, the microhardness of the as-deposited sample is higher than that of the annealed ones, and the microhardness values decrease with prolonging the annealing time. For the 25 mm sample, as shown in Fig. 7(b), the microhardness of as-deposited specimen is the lowest and the values increase slightly along the building direction. These curves of the annealed samples can be divided into 2 parts according to the microhardness value: 1) at lower half part of the sample, the microhardness increases along the building direction gradually; 2) at upper half part of the sample, the microhardness (>HV 500) is almost invariable and significantly higher than that of the

as-deposited sample (HV 411).

Apparently, the microhardness is closely related to the microstructure of the samples. For the 5 mm sample, the acicular  $\alpha'$  in the as-deposited specimen transforms to  $\alpha+\beta$  after annealing treatment, and the microhardness reduces with prolonging the time. The precipitation of fine  $\alpha_s$  is the main reason why the microhardness of the annealed 25 mm sample increases so much. At lower half part of the sample, the strengthening effect increases along the building direction because the amounts of  $\alpha_s$  increase with the increase of volume fraction of metastable  $\beta$  phase. The majority of upper half part of the as-deposited 25 mm sample is metastable  $\beta$  phase so that  $\alpha_s$  precipitates homogeneously after annealing treatment which makes the microhardness more close to each other. The little variation of microhardness of the samples with different annealing time is consistent with the small change in the microstructure.

### 3.4 Room temperature tensile properties

To release residual stress and keep strength of the specimens, the heat treatment of 600 °C, 1 h/FC was selected. The room temperature tensile properties of as-deposited and annealed specimens (average values of three specimens) are presented in Table 2. The mechanical properties of the as-deposited LAMed specimens are characterized by obvious anisotropy. The character of anisotropy has also been reported by other researchers [19,20]. The L-direction specimen shows the character of low strength but high ductility when compared with the T-direction specimen. After annealing treatments, the L-direction specimen is strengthened significantly accompanied by the reduction of ductility. The strength of the annealed T-direction specimen does not change, however, the ductility reduces notably.

**Table 2** Room temperature tensile properties of as-deposited and annealed specimens

Specimen	Direction	Ultimate tensile strength/MPa	Yield stress/MPa	Elongation/%	Area reduction/%
As-deposited	T	1225±7	1220±2	3.4±0.8	8.3±0.3
	L	1053±17	1030±26	14±1.5	42±2.8
Annealed	T	1230±4	1220±2	2.4±0.3	3±2
	L	1210±14	1180±1	3.8±0.3	10±1.8

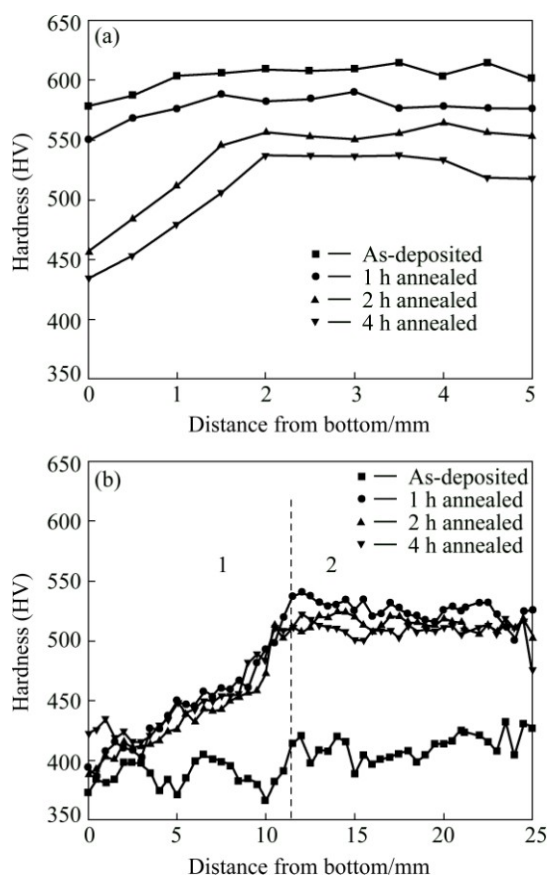


**Fig. 7** Microhardness of different samples along building direction: (a) 5 mm samples; (b) 25 mm samples

The SEM images of fracture surfaces and cross-sections through the fracture surfaces of the as-deposited T-direction and L-direction specimens are shown in Fig. 8. As shown in Fig. 8(a), the as-deposited T-direction specimen shows no apparent plastic deformation before fracture. It has mixed-rupture characteristics of trans-granular and inter-granular. The

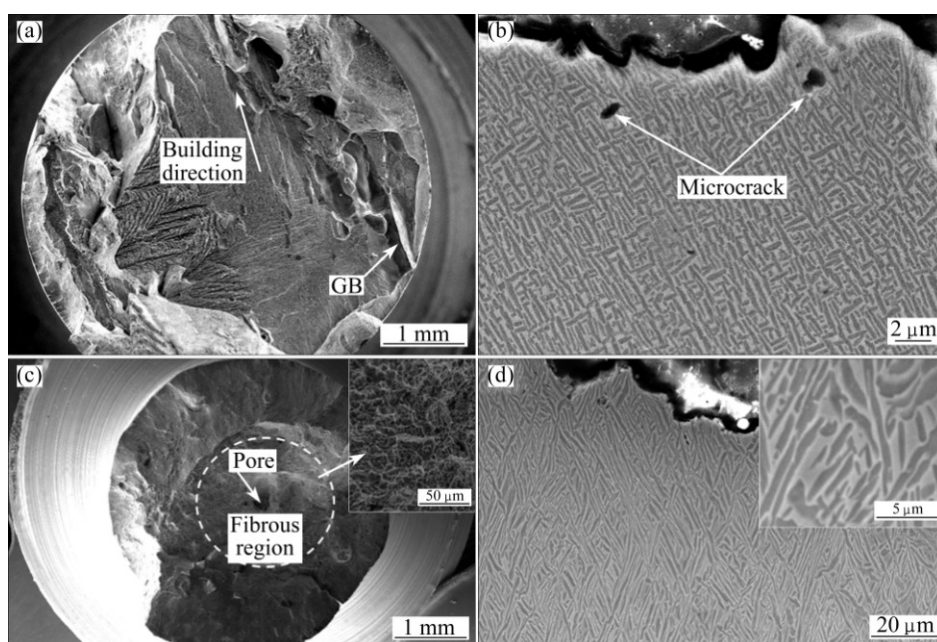


**Fig. 8** SEM images of fracture surfaces (a, c) and cross-sections (b, d) of T-direction as-deposited specimen (a, b) and L-direction as-deposited specimen (c, d)

grain boundary (GB) feature can be observed and indicated. The cross-section microstructure near the fracture is very fine rib-like  $\alpha$  phase (1–3  $\mu\text{m}$ ) and microcrack can be observed in Fig. 8(b). The microstructure is quite different from the 5 mm as-deposited specimen due to different thermal history caused by different sizes and shapes. The fracture of L-direction as-deposited specimen takes place at the location about 25 mm away from the bottom with extensive plastic deformation. It shows the characteristics of trans-granular fracture. As shown in Fig. 8(c), a pore at the center of the fracture surface may be the crack source. Besides, fibrous region and dimples feature can be observed. The microstructure near the fracture is panel-like  $\alpha_p$  with the length of 5–15  $\mu\text{m}$  (Fig. 8(d)) and no fine  $\alpha_s$  precipitates in the  $\beta$  matrix. Finer microstructure shows higher strength but poor ductility which can be explained by the fact that the onset of plastic deformation depends on the  $\alpha$  colony size (it equals the width of rib-like  $\alpha$  phase and panel-like  $\alpha_p$ ), and small colony size delays the onset of plastic deformation [21].

The SEM images of fracture surfaces and cross-sections through the fracture surfaces of the 1 h annealed T-direction and L-direction specimens are shown in Fig. 9. As shown in Fig. 9(a), the annealed T-direction specimen shows no necking and a mixed-rupture characteristic of trans-granular and inter-granular. Grain boundary feature can be observed both on the fracture surface and the cross-section. It can be seen that the  $\beta$  grains parallel to the building direction which is the

typical macrostructure characteristics of LAMed titanium alloy. According to the river pattern direction, the crack initiation at the grain boundary can be found. The microstructure near the fracture is fine rib-like  $\alpha$  phase (1–3  $\mu\text{m}$ ) which is similar to the as-deposited specimen. However, between the rib-like  $\alpha$  phase, the extremely fine  $\alpha_s$  can be observed (Fig. 9(c)) which is different from the as-deposited specimen.

Figure 9(d) shows the topography of fracture surface of the annealed L-direction specimen and the crack source is indicated. The annealed L-direction specimen exhibits different appearance when compared with the as-deposited one. The microstructure near the fracture consists of coarse  $\alpha_p$  and fine  $\alpha_s$  (Fig. 9(e)). It can be seen from Fig. 9(f) that microcrack forms along the interface of  $\alpha_p$  and  $\beta$  matrix. The existence of  $\alpha_p$  has no obvious effect on changing the path of crack propagation.

The different properties of these specimens are due to the presence of different microstructures. As discussed above, the microstructure of LAMed Ti–5Al–2Sn–2Zr–4Mo–4Cr alloy depends on the thermal history. The differences on fabrication path and shape of L-direction and T-direction specimens will affect the thermal history. So, the microstructure characteristics of L-direction and T-direction specimens are obvious different, as shown in Figs. 8 and 9.

The high strength is usually associated with the fine nature of  $\alpha$  phase which is equivalent to a small grain size. For the as-deposited T-direction specimens, the microstructure consists of very fine rib-like  $\alpha$  phase.

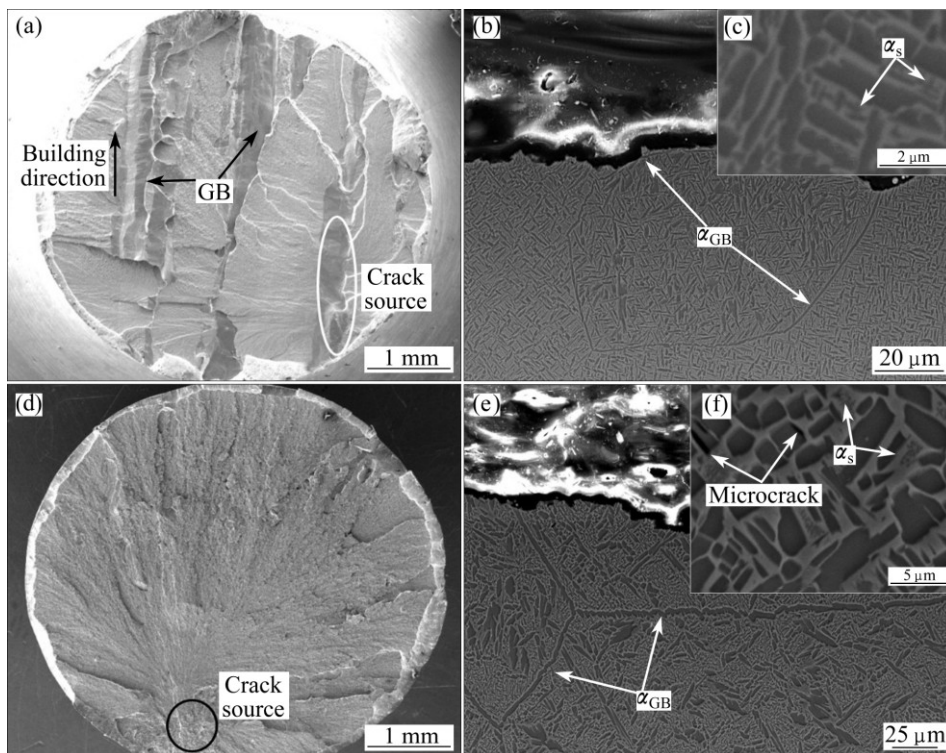


**Fig. 9** SEM images of fracture surfaces (a, d) and cross-sections (b, c, e, f) of T-direction (a–c) and L-direction (d–f) annealed specimens

Usually, the grain boundary strength is superior to the grain strength, so the fracture mechanism is trans-granular at room temperature. However, the fine rib-like  $\alpha$  phase improves the grain strength significantly and results in that the grain strength is superior to the grain boundary strength, so the cracks tend to initiate and expand along the grain boundary  $\alpha$  layers. For the as-deposited L-direction specimens, there is almost no  $\alpha_s$  precipitated and the size of panel-like  $\alpha$  phase is much bigger. So, it is much easier to deform plastically. This may be the main reason why the L-direction specimen exhibits high ductility but low strength compared with the T-direction specimen.

Though the strength of the annealed T-direction specimen does not change, the ductility reduces notably due to the precipitation of  $\alpha_s$ , and the tendency of inter-granular fracture increases. But for the annealed L-direction specimen, the microstructure consists of larger but irregular  $\alpha$  phase and unevenly distributed  $\alpha_s$  compared with the T-direction specimen. Crack initiation occurs along the interface of  $\alpha$  phase and  $\beta$  matrix due to dislocation pileup. Furthermore, prior  $\beta$  phase has a dominant (100) solidification texture along the building direction and keeps consistence after annealing treatment [22,23]. Therefore, grain orientation may play an important role on the path of crack propagation since the principal stress of T-direction specimen is perpendicular to the  $\beta$  columnar crystal, so crack is easy

to expand along the grain boundary [18].

## 4 Conclusions

1) The microstructure characteristics of the as-deposited specimens along the building direction are strongly affected by the thermal history of LAM process. At the bottom of 5 mm sample, very fine basketweave  $\alpha$  phase can be observed; while martensite  $\alpha'$  can be observed at the top of the sample. At lower half part of the 25 mm sample, both the  $\alpha_p$  and  $\alpha_s$  can be obtained; while at upper half part, no  $\alpha$  phase is observed.

2) The annealing treatment can promote the martensite  $\alpha'$  and retained  $\beta$  phase transforming to  $\alpha+\beta$ . For the 5 mm sample, the martensite  $\alpha'$  transforms to rib-like  $\alpha$  and reduces the microhardness. For the 25 mm sample, acicular  $\alpha_s$  precipitates from the retained  $\beta$  phase and increases the microhardness.

3) The room temperature tensile properties of the as-deposited LAMed specimens are characterized of obvious anisotropy. The as-deposited L-direction specimen shows the character of low strength but high ductility when compared with the as-deposited T-direction specimen. After annealing treatment, L-direction specimen is strengthened significantly accompanied by the reduction of ductility. The strength of the annealed T-direction specimen does not change, however, the ductility reduces obviously.

## References

- [1] CHANDLER H. Heat treater's guide: Practices and procedures for nonferrous alloys [J]. Materials Park, OH: ASM International, 1996: 514.
- [2] LI Hong, ZHANG Chao, LIU Hong-bin, Li Miao-quan. Bonding interface characteristic and shear strength of diffusion bonded Ti-17 titanium alloy [J]. Transactions of Nonferrous Metals Society of China, 2015, 25(1): 80–87.
- [3] QIAN Ting-ting, LIU Dong, TIAN Xiang-jun, LIU Chang-meng, WANG Hua-ming. Microstructure of TA2/TA15 graded structural material by laser additive manufacturing process [J]. Transactions of Nonferrous Metals Society of China, 2014, 24(9): 2729–2736.
- [4] LI Zhen, TIAN Xiang-jun, TANG Hai-bo, WANG Hua-ming. Low cycle fatigue behavior of laser melting deposited TC18 titanium alloy [J]. Transactions of Nonferrous Metals Society of China, 2013, 23(9): 2591–2597.
- [5] GRIFFITH M L, SCHLIENGER M E, HARWELL L D, OLIVER M S, BALDWIN M D, ENSZ M T, ESSIEN M, BROOKS J, ROBINO C V, SMUGERESKY J E, HOFMEISTER W H, WERT M J, NELSON D V. Understanding thermal behavior in the LENS process [J]. Materials and Design, 1999, 20: 107–113.
- [6] KOBRYN P A, SEMIATIN S L. The laser additive manufacture of Ti-6Al-4V [J]. JOM-US, 2001, 53(9): 40–42.
- [7] KOBRYN P A, MOORE E H, SEMIATIN S L. The effect of laser power and traverse speed on microstructure, porosity, and build height in laser-deposited Ti-6Al-4V [J]. Scripta Materialia, 2000, 43: 299–305.
- [8] ZHANG Qiang, CHEN Jing, GUO Peng-fei, TAN Hua, LIN Xin, HUANG Wei-dong. Texture and microstructure characterization in laser additive manufactured Ti-6Al-2Zr-2Sn-3Mo-1.5Cr-2Nb titanium alloy [J]. Materials and Design, 2015, 88: 550–557.
- [9] BRANDL E, PALM F, MICHAÏLOV V, VIEHWEGER B, LEYENS C. Mechanical properties of additive manufactured titanium (Ti-6Al-4V) blocks deposited by a solid-state laser and wire [J]. Materials and Design, 2011, 32: 4665–4675.
- [10] BAUFELD B. Effect of deposition parameters on mechanical properties of shaped metal deposition parts [J]. Proceedings of the Institution of Mechanical Engineers, Part B: Journal of Engineering Manufacture, 2012, 226: 126–136.
- [11] ZHU Yan-yan, LIU Dong, TIAN Xiang-jun, TANG Hai-bo, WANG Hua-ming. Characterization of microstructure and mechanical properties of laser melting deposited Ti-6.5Al-3.5Mo-1.5Zr-0.3Si titanium alloy [J]. Materials and Design, 2014, 56: 445–453.
- [12] KELLY S M. Microstructural evolution in laser-deposited multilayer Ti-6Al-4V builds: Part I. Microstructural characterization [J]. Metallurgical and Materials Transaction A, 2004, 35: 1861–1867.
- [13] KELLY S M. Microstructural evolution in laser-deposited multilayer Ti-6Al-4V builds: Part II. Thermal modeling [J]. Metallurgical and Materials Transaction A, 2004, 35: 1869–1879.
- [14] LIU Chang-meng, TIAN Xiang-jun, TANG Hai-bo, WANG Hua-ming. Microstructural characterization of laser melting deposited Ti-5Al-5Mo-5V-1Cr-1Fe near  $\beta$  titanium alloy [J]. Journal of Alloy and Compounds, 2013, 572: 17–24.
- [15] LÜTJERING G, WILLIAMS J C. Titanium [M]. Berlin: Springer, 2007: 203–332.
- [16] JIA Wen-peng, LIN Xin, TAN Hua, YANG Hai-ou, ZHONG Cheng-wen, HUANG Wei-dong. Numerical simulation for temperature field of TC4 titanium alloy hollow blade during laser rapid process [J]. Rare Metal Materials and Engineering, 2007, 36: 1193–1199.
- [17] ZHU Yan-yan, LI Jia, TIAN Xiang-jun, WANG Hua-ming, LIU Dong. Microstructure and mechanical properties of hybrid fabricated Ti-6.5Al-3.5Mo-1.5Zr-0.3Si titanium alloy by laser additive manufacturing [J]. Materials Science and Engineering A, 2014, 607: 427–434.
- [18] SAUER C, LUETJERING G. Thermo-mechanical processing of high strength  $\beta$ -titanium alloys and effects on microstructure and properties [J]. Journal of Materials Process Technology, 2001, 117: 311–317.
- [19] MOK S H, BI G, FOLKES J, PASHBY I. Deposition of Ti-6Al-4V using a high power diode laser and wire, Part I: Investigation on the process characteristics [J]. Surface and Coatings Technology, 2008, 202: 3933–3939.
- [20] CARROLL B E, PALMER T A, BEESE A M. Anisotropic tensile behavior of Ti-6Al-4V components fabricated with directed energy deposition additive manufacturing [J]. Acta Materialia, 2015, 87: 309–320.
- [21] SIMONELLI M, TSE Y Y, TUCK C. Effect of the build orientation on the mechanical properties and fracture modes of SLM Ti-6Al-4V [J]. Materials Science and Engineering A, 2014, 616: 1–11.
- [22] SIMONELLI M, TSE Y Y, TUCK C. On the texture formation of selective laser melted Ti-6Al-4V [J]. Metallurgical and Materials Transactions A, 2014, 45: 2863–2872.
- [23] AL-BERMANI S S, BLACKMORE M L, ZHANG W, TODD I. The origin of microstructural diversity, texture, and mechanical properties in electron beam melted Ti-6Al-4V [J]. Metallurgical and Materials Transactions A, 2010, 41: 3422–3434.

## 激光增材制造 Ti-5Al-2Sn-2Zr-4Mo-4Cr 合金的 显微组织演化及力学性能

张强, 陈静, 谭华, 林鑫, 黄卫东

西北工业大学 凝固技术国家重点实验室, 西安 710072

**摘要:** 研究激光增材制造 Ti-5Al-2Sn-2Zr-4Mo-4Cr 合金的显微组织演化、维氏硬度及室温拉伸性能。结果表明: 激光增材制造过程的热历史显著影响显微组织演化。在试样的不同沉积高度位置可以观察到不同形貌的初生  $\alpha$  相、细小次生  $\alpha$  相及马氏体相。退火处理可以促使短棒状  $\alpha$  相或细小次生  $\alpha$  相析出, 从而降低或增加维氏硬度。L 方向和 T 方向拉伸试样相组成相同但形貌不同。沉积态试样室温拉伸时表现出明显的各向异性。L 方向拉伸试样的强度低但塑性好, T 方向拉伸试样相反。经退火处理之后, L 方向拉伸试样的强度增加但塑性显著降低; T 方向拉伸试样的强度无明显变化而塑性降低 50%。

**关键词:** Ti-5Al-2Sn-2Zr-4Mo-4Cr 合金; 激光增材制造; 显微组织; 热历史; 力学性能

(Edited by Mu-lan QIN)